Very high cycle fatigue (VHCF) response of an Additively manufactured Nitinol

International Journal of Fatigue 200 (2025) 109130

Contents lists available at ScienceDirect

International Journal of Fatigue

journal homepage: www.elsevier.com/locate/ijfatigue

Very high cycle fatigue (VHCF) response of an Additively manufactured Nitinol☆

C. Boursier Niutta [a,*], A.P. Pagnoncelli [b], A. Tridello [a], J. Fiocchi [c], C.A. Biffi [c], A. Tuissi [c], D.S. Paolino [a]

[a] Department of Mechanical and Aerospace Engineering, Politecnico di Torino, 10129 Turin, Italy
[b] University Sustainability, Research Infrastructures and Laboratories, Politecnico di Torino, 10129 Turin, Italy
[c] CNR ICMATE– Institute of Condensed Matter Chemistry and Technologies for Energy, Via Previati 1/E, 23900 Lecco, Italy

ARTICLE INFO

Keywords:
Nitinol shape memory alloy
Additive manufacturing
Very high cycle fatigue
Ultrasonic testing

ABSTRACT

This work investigates the Very High Cycle Fatigue (VHCF) response of an Additively Manufactured (AM) Nitinol alloy. To resemble in-service loading conditions of typical Nitinol components, an innovative experimental setup has been proposed, where the martensite/austenite transformation fraction is controlled by applying a mean static compressive load through an electrodynamic machine, and the partially transformed material is fatigued up to 10^9 cycles through an ultrasonic machine. Hourglass-shaped hollow specimens have been designed by means of a Finite Element (FE) iterative procedure to account for the material phase transformation with applied stress. The FE model has been optimized by considering the displacement field acquired with a high-speed camera, to ensure a reliable computation of the applied stress amplitude. With the proposed setup, the partially transformed AM Nitinol alloy has been subjected to VHCF tests. FE analyses on Representative Volume Elements (RVEs) with defect size determined through μ-CT scans have been also performed to analyze the failure driving force.

1. Introduction

Nitinol is the most well-known and widely used shape memory alloy (SMA) [1,2]: depending on its composition and thermal–mechanical state, it may present shape memory or super-elastic behavior, i.e. the ability to recover permanent deformation upon heating or unloading, respectively. Both such effects depend on the characteristic diffusionless transformation between the cubic austenitic (B2) and monoclinic martensitic (B19′) phases [3]. Nitinol alloy accordingly meets the needs of several challenging fields, including the biomedical and aerospace sectors. The possibility of producing such material through advanced processing techniques, such as Additive Manufacturing (AM), is currently attracting considerable interest in the scientific community, owing to the possibility of bringing together the peculiar thermal–mechanical properties of Nitinol and the well-established advantages of AM, being the design freedom and the improved lightness and functionality of components [4,5]. AM process allows the use of topology optimization methods for the design of Nitinol components [6,7], to achieve better mechanical performance at reduced weight and material waste compared to standard manufacturing processes, without contrasting the manufacturing feasibility. Laser powder bed fusion (LPBF) is one of the most established AM processes, and its use in the production of Nitinol components is being actively researched. In this respect, it shall be observed that a main concern related to LPBF is the generation of defects during the process, which include lack of fusion and gas porosities, cold and hot cracks, as well as a range of different surface defects [8]. Although the nature, size and distribution of such defects can be effectively limited through proper process optimization or by dedicated post-processing techniques, their presence cannot be completely avoided and must be thus coped with.

This point is of particular interest in the case of Nitinol components, such as medical implants, which are subjected to relatively small cyclic loadings repeated several million times during the in-service life [9]. For example, coronary stents made of Nitinol alloy are likely to exceed 300

☆ This article is part of a special issue entitled: 'Fatigue at VHCF9' published in International Journal of Fatigue.

* Corresponding author.
E-mail addresses: carlo.boursier@polito.it (C. Boursier Niutta), ana.pagnoncelli@polito.it (A.P. Pagnoncelli), andrea.tridello@polito.it (A. Tridello), jacopo.fiocchi@cnr.it (J. Fiocchi), carloalberto.biffi@cnr.it (C.A. Biffi), ausonio.tuissi@cnr.it (A. Tuissi), davide.paolino@polito.it (D.S. Paolino).

https://doi.org/10.1016/j.ijfatigue.2025.109130
Received 31 December 2024; Received in revised form 3 April 2025; Accepted 24 June 2025
Available online 25 June 2025

Table 1
Main process parameters used for processing niti samples.

Laser power	Exposure time	Oxygen level	Atmosphere	Layer thickness	Hatch/point distance	Laser spot size
150 W	75 μs	< 20 ppm	Argon	30 μm	50 / 120 μm	65 μm

million cycles in ten years of operation. Accordingly, the Very High Cycle Fatigue (VHCF) response of such material must be properly assessed. Weaver et al. [9] first addressed the VHCF of Nitinol alloy by performing rotary bending tests on wire-shape specimens. Moreover, in typical applications, the Nitinol alloy can be subjected to a pre-stress loading condition with a partial austenite/martensite phase change and the fatigue phenomenon occurs in the phase transformation stage [2,10,11]. To the best of the authors' knowledge, this aspect has not been addressed yet, and the literature remains relatively scarce. The goal of this work is thus to investigate the VHCF response of the shape memory Nitinol alloy in the phase transformation region to resemble the in-service loading conditions.

The VHCF characterization is generally addressed at ultrasonic frequency, i.e., 20 kHz, to attain results up to 10^9-10^{10} cycles in reasonable testing time. By means of initially preloaded thin sheet Nitinol specimens, Fitzka et al. [12,13] first showed the general applicability of the ultrasonic testing technique to Nitinol. Ultrasonic testing technique also offers several advantages for Nitinol testing, such as the intrinsic displacement-controlled setup which replicates the duty cycle of most Nitinol components, and the absence of grippers which can induce a phase transformation and, accordingly, affect the results [14,15].

We propose an innovative testing setup and procedure to perform axial ultrasonic fatigue tests while inducing the partial phase transformation through a mean static load. With respect to standard ultrasonic setups, the specimen has been here mounted between two horns and, in correspondence of the nodal lines of the vibrating system, the setup is constrained to an electro-dynamic testing machine, through which the mean compressive load is applied. The mean compressive load allows to control the martensite/austenite transformation fraction, while the cyclic loading is applied by the ultrasonic machine. Moreover, the variable material properties due to the phase change challenge the standard procedures of specimen and setup design for axial ultrasonic fatigue tests. The phase change indeed involves a variation of the elastic properties of the material with the applied stress. After characterizing the material super-elastic behavior through quasi-static compressive tests, an iterative Finite Element (FE) procedure has been considered for the identification of the geometrical characteristics of an hourglass-shaped specimen.

To compute the stress amplitude during the ultrasonic test, the FE model has been optimized to replicate the displacement field within the specimen recorded with a high-speed camera, thus characterizing the material elastic properties in the ultrasonic testing conditions. After assessing the defect population through μ-CT scans, VHCF tests have been performed with the proposed setup and testing procedure. Finally, by means of an FE analysis on defective Representative Volume Elements (RVEs), the failure driving force has been analyzed.

The paper is organized as follows: Section 2 describes the AM process, the resulting material characteristics and the proposed experimental setup. In Section 3, the FE iterative procedure is described, and the specimen design is presented. Section 4 is dedicated to the validation of the iterative procedure and to the FE model optimization. Results of the μ-CT scans and of the VHCF tests are reported in Section 5 and discussed in Section 6. Conclusions are finally given.

2. Materials and methods

In this section, material properties are first presented. The VHCF setup and testing procedure to induce and control the martensite/austenite transformation fraction are then described.

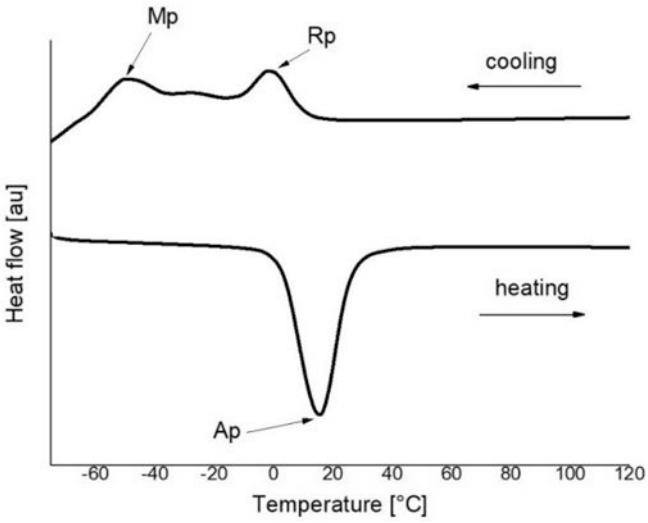

Fig. 1. DSC scan of the Nitinol sample in heat treated condition.

2.1. AM process and material characteristics

Spherical Ni56Ti46 (wt.%) gas-atomized powder, having a mesh size ranging from 15 μm up to 63 μm and produced by Nanoval, has been used in this work. Different samples have been produced by an LPBF system (mod. AM 400 from Renishaw, UK), which controls the exposure time and in accordance with the process parameters listed in Table 1.

Process parameters have been optimized in a previous work [16] on small cubic samples, with the aim of maximizing the relative density of the produced samples (above 99.5 %), while accounting for the required functional properties, by varying the laser power and the exposure time.

Samples have been also subjected to thermal treatments consisting of a 5′ holding at 500 °C in air, followed by water quenching to ambient temperature. Mechanical treatments for reducing the surface roughness have not been applied.

The transformation temperatures have been detected by Differential Scanning Calorimetry (DSC, mod. Q25 from TA Instruments, USA); the measurements have been carried out on small samples (about 25 mg in weight) with a heating/cooling rates of 10 °C/min in the temperature range [-75 °C; 120 °C] and are reported in Fig. 1.

It can be observed that upon heating the reverse martensitic transformation, passing from martensite to austenite, takes place in a single-stage phase transformation at a peak temperature (indicated as Ap) of 15 °C. On the contrary, upon cooling the phase transformation from austenite to martensite is detected in a double stage: the transformation from austenite to R-phase has the peak temperature (indicated as Rp) at 0 °C, while the transformation from R-phase to martensite (indicated as Mp) at −50 °C.

Accordingly, the Nitinol alloy subjected to the described thermal treatment is in austenite phase at room temperature.

Quasi-static compression tests have been conducted on cylindrical specimens of 7 mm diameter through a servo-hydraulic machine (Instron 8801) at a constant crosshead rate of 1 mm/min for: i) determining the alternate and average stress components that prevent the phase transformation during the ultrasonic cyclic load; ii) a first estimation of the Young's modulus of the partially transformed material. Strains have been computed by post-processing the displacement data acquired on

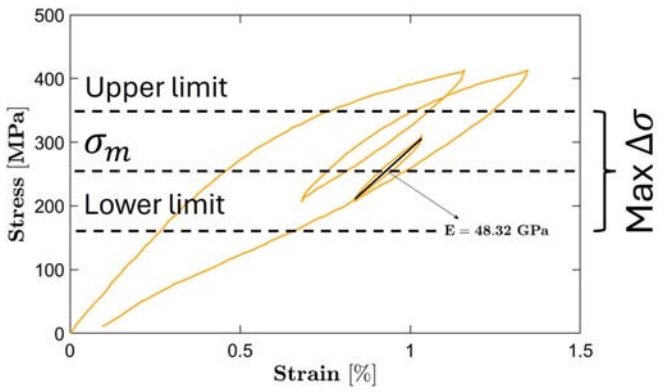

Fig. 2. Quasi-static compressive stress–strain curve of the AM Nitinol for the identification of the upper and lower stress limits of the transition region and the evaluation of the elastic modulus within the transformation region.

Table 2
Average material properties determined through the conducted tests.

Elastic Modulus [GPa] (Dynamic tests)	Elastic Modulus [GPa] (Compression tests)	Density [kg/m^3]
62.2	60.4	6380

the specimen surface with the Digital Image Correlation (DIC) technique. As the VHCF tests must be conducted in the transition region, where part of the material is transformed from austenite to martensite phase, the quasi-static compressive tests have been performed by loading and unloading the material to identify the upper and lower limits of the hysteresis cycle. Moreover, an estimate of the elastic modulus has been determined by unloading and reloading the specimen in the transition region, as shown in Fig. 2.

As shown, two loading and unloading cycles have been performed. The first loading–unloading cycle highlights that the stress level of about 400 MPa has been achieved at the beginning of the unloading phase for a strain of 1.1 % and, after loading, at 1.25 %. This suggests that the material has experienced further austenite–martensite transformation, likely above 360 MPa, where the stress–strain slope significantly changes along the reloading path. Instead, after completing the second loading–unloading cycle, the same strain level, i.e., 0.75 %, is achieved. As such, while unloading to 210 MPa, the material has not experienced the reverse transformation of martensite into austenite. Proceeding along the unloading path, the stress–strain slope changes at about 160 MPa, which can be retained as the stress at which the reverse transformation begins, as shown in Fig. 2. From these loading–unloading cycles, the stress range $\Delta\sigma$, that prevents the phase transformation in the fatigue test for the average stress σ_m of 265 MPa, i.e. the average stress of the second loading–unloading cycle of Fig. 2, has been determined to be equal to 200 MPa, as highlighted in Fig. 2. Moreover, from the loading and unloading path, the elastic modulus in the transformation region has been computed, showing a decrease from 60.4 GPa of the pure austenite to 48.3 GPa, due to the austenite conversion into martensite.

Finally, for a preliminary assessment of the material response in dynamic conditions, the dynamic properties have been determined by means of the Impulse Excitation Technique (IET), in accordance with the standard ASTM E1816 [17]. The average Young's modulus results are reported in Table 2.

Table 2 highlights the limited discrepancy between dynamic and quasi-static properties. Moreover, although the material Young's modulus in the pure austenite phase is in accordance with values reported in the literature for specimen manufactured through traditional processes, a sound comparison cannot be addressed as percentages of Nickel and Titanium and crystals size also play a key role in the mechanical response. In addition, the AM process inherently induces porosities, as will be shown later, which can also affect the elastic response.

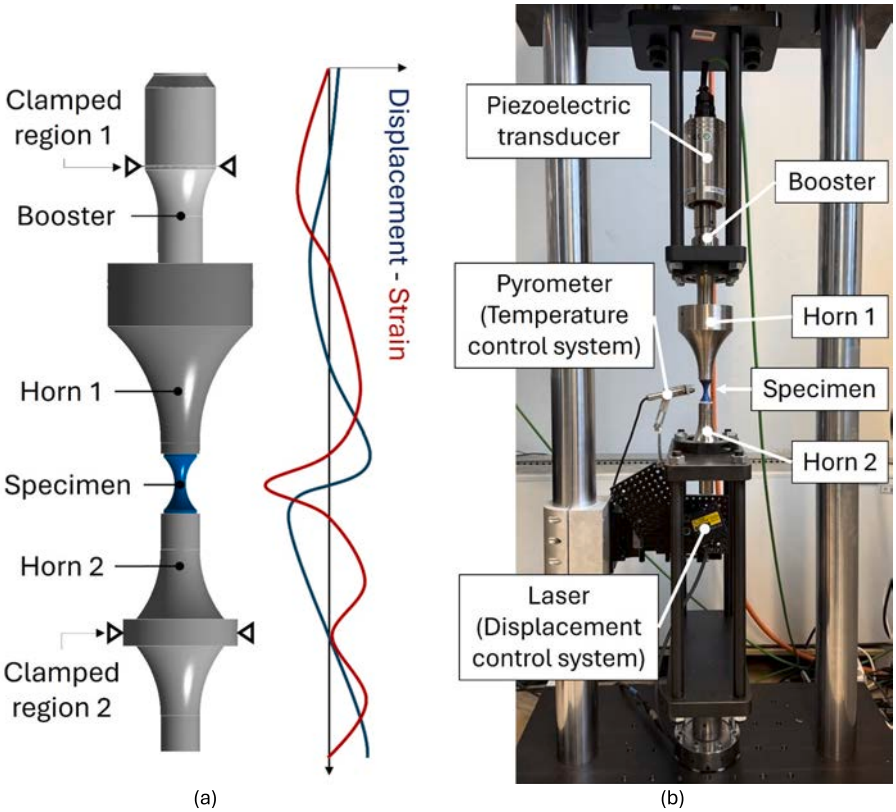

Fig. 3. Testing configuration: a) functioning scheme; b) experimental setup.

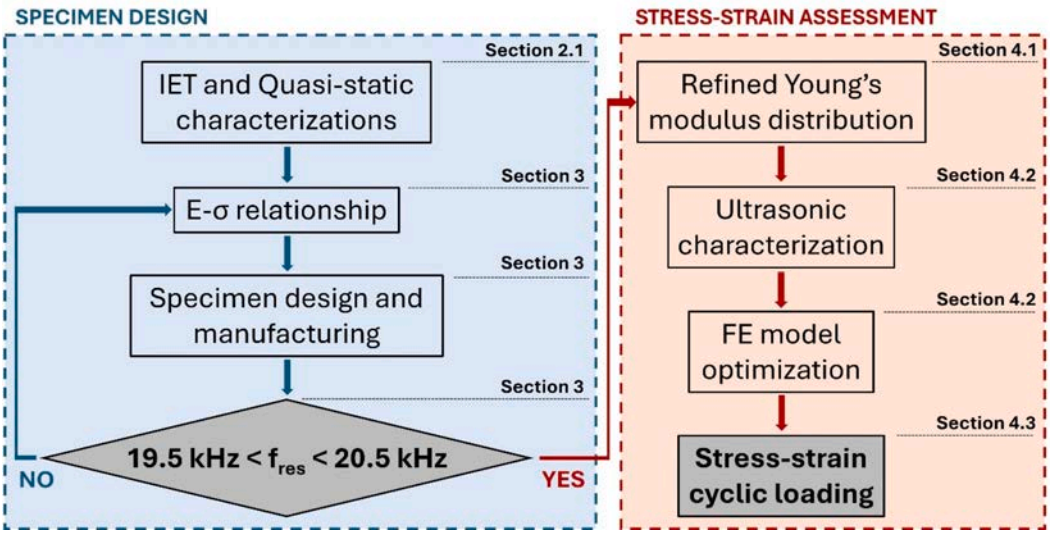

Fig. 4. Flowchart of the methodology for the specimen design and cyclic loading assessment.

2.2. VHCF setup

To resemble the in-service loading conditions of typical biomedical applications, that is the material is subjected to the cycling loading in the transition phase stage, a specifically designed setup has been developed. The proposed test setup allows to perform axial ultrasonic fatigue tests, to achieve the VHCF response in acceptable testing time, while a static mean load is applied on the specimen to induce and control the partial phase change. Fig. 3 reports a scheme and a picture of the experimental setup.

All the components of the setup and the specimen have been designed to be in longitudinal resonance at 20 kHz. The input displacement amplitude generated by a piezoelectric transducer is transmitted through a booster to the first horn, which further amplifies it to the specimen. In the adopted setup, the booster and the upper horn have an amplification factor of 2 and 5, respectively. At the free-end of the second horn, the displacement is monitored through a laser system to realize a closed-loop control of the applied cyclic load. The specimen is glued to the two horns to guarantee vibration wave continuity.

In correspondence of the nodal lines of the booster and of the second horn, the setup is constrained to an electro-dynamic StepLab testing machine, equipped with a 30 kN load cell, and through which the mean compressive load is applied. More in detail, to induce the same partial phase change of the preliminary quasi-static tests and mantain the identified upper and lower limits (see Fig. 2), thus avoiding further phase transformation in the fatigue tests, the following loading procedure has been adopted in load-controlled configuration and with a constant rate of 1 mm/min: i) the specimen is compressed up to 420 MPa and load is maintained for 30s to permit the complete austenite/martensite transformation; ii) the load is reduced to 210 MPa and maintained for 30s; iii) the compressive load is increased up to 265 MPa and held during the ultrasonic vibration.

As in the austenite/martensite phase change the hysteresis cycle dissipates consistent amount of energy into heating, especially at ultrasonic frequency. An infrared sensor has been adopted to control the temperature on the specimen surface within a suitable range. That is, when the temperature exceeded the maximum allowable value, i.e., 40 °C in this work, the test was paused and restarted when its value fell below 36 °C. A cooling air system has been adopted to speed up the refrigeration. An effective frequency of 2000–3000 Hz, depending on the testing strain amplitude, has been achieved.

Finally, it is worth noticing that the proposed setup can be adopted even for the application of mean tensile load. However, the use of glue for joining the specimen to the horns can be critical and other connections, such as by screwing the specimen, can be considered.

2.3. Methodology for specimen design and cyclic loading characterization

The variable material properties with the applied stress as result of the phase transformation challenge the standard procedures of specimen design and characterization of the applied cyclic loads.

The methodology adopted in this work is schematically depicted in Fig. 4.

The flowchart also includes the Sections addressing each topic for ease of reading. Starting from the preliminary characterizations through the IET and the quasi-static tests, the elastic modulus variation with the applied load can be estimated and the specimen can be designed to longitudinally resonate at 20 kHz. In this work, the specimen design has been addressed by means of an iterative FE procedure, as will be detailed in Section 3. If the resonant frequency of the 3D printed specimen is indeed comprised between 19.5 kHz and 20.5 kHz, that is the frequency working range of the machine, the assessment of the cyclic loading can be addressed, otherwise the specimen must be redesigned with a new estimation of the relationship between the Young's modulus and the applied stress. For assessing the stress–strain cyclic loading conditions of the specimen, the Young's modulus variation with the applied stress, that corresponds to the austenite/martensite fraction along the designed specimen, must be accurately determined, as geometrical features and testing conditions can affect the elastic response of Nitinol alloy. In particular, the Young's modulus must be determined in the ultrasonic loading conditions, i.e. the dynamic Young's modulus, to account for strain rate effects, microstructural changes due to the oscillating load and self-heating effects. While the self-heating has been limited by controlling the specimen temperature during the test and its influence on the phase transformation can be accordingly neglected, the effect of the dynamic loading condition on the phase transformation must be evaluated. Indeed, experimental observations [10,18] have shown a consistent increase of the Young's modulus, when subjected to strain-controlled loading conditions. This phenomenon, that also comes with a decrease in the hysteresis width and has been attributed to microstructural changes of the martensite phase dispersion [18], determines a concomitant increase in stress range, which must be properly assessed. In this work, a high-speed camera has been adopted to assess the displacement field along the specimen during the ultrasonic tests, as will be detailed in Section 4.2. By optimizing the FE model to mimic the ultrasonic loading conditions and by calibrating the strain amplitude to

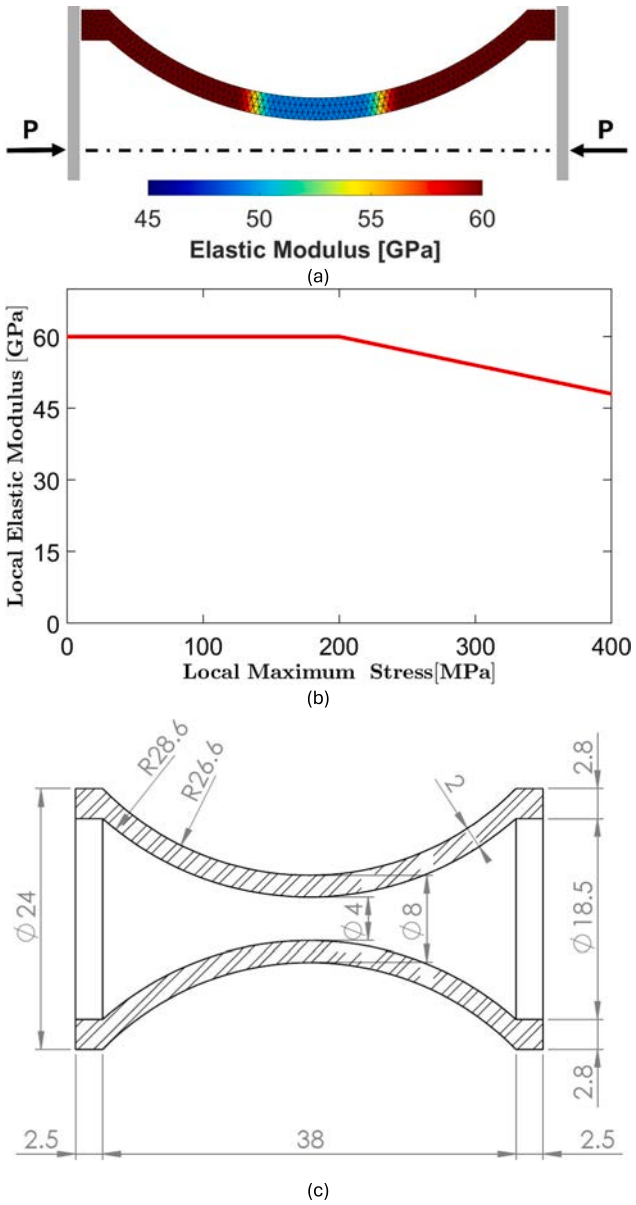

Fig. 5. Design of the Nitinol specimen: a) FE model with variable elastic properties; b) Assumed elastic modulus variation with the applied load; c) geometrical features of the identified specimen.

the input voltage exerted by the piezoelectric actuator, the stress–strain cyclic loading can be accurately determined.

3. Specimen design

The specimen has been designed to satisfy the following constraints: i) the longitudinal resonance frequency must be in the working range of the machine, i.e., comprised between 19.5 and 20.5 kHz; ii) the specimen height must be smaller than 55 mm as limited by the printing machine; iii) the cross-section must be designed in accordance with the testing procedure defined in Section 2.2 and the load cell limitation of the StepLab testing machine; iv) inelastic buckling response must be avoided; v) the ratio between the strain amplitude at the specimen center and the input displacement at the specimen extremes must be maximized to extend the range of investigation with the ultrasonic machine.

The standard procedure of specimen design for VHCF ultrasonic tests is however challenged by the material phase transformation, which involves a variation of the elastic properties of the material with the applied stress, thus affecting the longitudinal resonance frequency and the compressive response. An iterative procedure has been considered for the identification of the geometrical characteristics of an hourglass-shaped specimen. The specimen has been designed by means of FE modal analysis in LS-Dyna environment, performed in the configuration deformed by the compressive mean load. Shell elements with axisymmetric formulation have been retained to reduce the computational cost. To account for Young's modulus variation along the specimen axis, each shell element has been assigned to a specific part with individual elastic property. It has been assumed that the Young's modulus is constant and equal to 60 GPa up to 200 MPa and linearly varies from 60 GPa to 48 GPa with the applied stress between 200 MPa and 400 MPa, as observed in the quasi-static test (see Fig. 2). Each element is thus subjected to a different linear elastic material law. In the FE simulation, the mean compressive load is first applied, and the stress of each element is determined. The Young's moduli of each element are then determined according to the assumed variation curve. In a new FE run, the compressive load is applied, and the modal analysis is performed in the deformed configuration of the specimen, to extract the longitudinal resonance frequency.

To satisfy all the constraints, an hourglass-shaped with hollow cross section has been considered. The hourglass shape indeed allows to increase the stress-to-input displacement ratio with respect to a standard straight tubular specimen, and to localize the phase transformation in a limited central region, with respect to straight and dogbone geometries. By localizing the phase transformation in the central portion of the specimen, the influence of the retained assumptions, such as the linear variation of the Young's modulus with the applied stress, is also circumscribed.

Fig. 5a shows the FE model, where different colors of shell elements highlight the variable material properties. In Fig. 5b, the curve describing the variation of the Young's modulus with the applied stress is reported. Finally, the identified specimen geometry is reported in Fig. 5c.

The resulting longitudinal resonant frequency was equal to 20.0 kHz and, according to FE modal analysis, the ratio between the strain amplitude and the input displacement was 81.4 με/μm, that is, the maximum strain amplitude for the retained setup configuration is 8140 με. The buckling occurrence has been verified through a dedicated buckling analysis, conservatively assuming a constant Young's modulus of 20 GPa, as if the martensite transition occurred in all the specimen.

It is worth remarking that the methodology adopted for the specimen design assumes that the Young's modulus linearly varies with the applied stress. Accordingly, the strain amplitude computed with the FE model must be verified through a dedicated strain gauge calibration. Moreover, to determine the corresponding stress amplitude, the Young's modulus of the partially transformed material must be assessed while accounting for the effect of the ultrasonic strain rate, of the cycling loading and of the temperature increase due to the self-heating of the material at ultrasonic frequency, which are known in the literature [10,19,20] to play a significant role on the phase transformation and, accordingly, on the resulting Young's modulus. The proper identification of the Young's modulus during the ultrasonic test, i.e., the dynamic Young's modulus, and its variation along the specimen is fundamental to assess the stress amplitude during the fatigue tests. The experimental approach for determining the dynamic Young's modulus and the stress amplitude in the manufactured specimen is described in Section 4.

4. Stress–strain cyclic loading

The experimental setup described in Section 2.2 allows ultrasonic fatigue tests in displacement-controlled configuration. Accordingly, the strain field is also controlled during the ultrasonic test. In the assumption of linear elasticity, the stress amplitude can be computed from the applied strain field. In the case of a Nitinol alloy tested in the transition

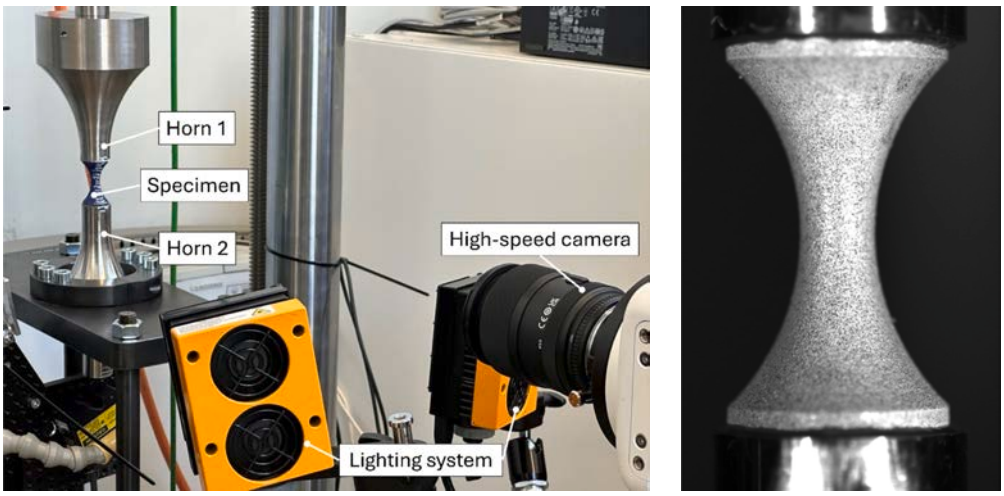

Fig. 6. Assessment of the stress–strain cyclic loading: a) setup with high-speed camera for displacement field acquisition; b) speckled specimen for the strain acquisition in the pre-loading quasi-static cycle.

region, it is, however, necessary to properly assess the dynamic Young's modulus of the partially transformed material and its variation along the specimen.

The dynamic Young's modulus and the resulting stress field in the ultrasonic loading condition have been here determined by optimizing the FE model described in Section 3. The optimization problem aimed at identifying the dynamic Young's moduli along the specimen by minimizing the discrepancy between the displacement field acquired with a high-speed camera (Photron Fastcam Nova S6) during the ultrasonic test and the displacement field computed by the FE model. Tracking points have been defined along the specimen with a step of 1 mm. Sampling frequency of the high-speed camera has been set to 250 kfps for a frame size of 128x16 pixel. For robustness, the displacement field has been acquired at increasing input voltages exerted by the piezoelectric actuator and all results at increasing voltages have been considered in the optimization process.

As for the Young's modulus variation with the applied mean stress, it has been assumed that its variation along the specimen axis is the same in quasi-static and ultrasonic loading conditions. Accordingly, the variation curve has been identified in the quasi-static pre-loading cycle. A Digital Image Correlation (DIC) analysis has been performed by means of the open-source software DICe to evaluate the strain field in the specimen and determine the stress–strain curves of each spot of the specimen.

Fig. 6a shows the setup for the acquisition of the displacement field at ultrasonic frequency, while Fig. 6b shows the speckled specimen for the strain acquisition in the pre-loading quasi-static cycle.

It is worth remarking that the pronounced hourglass shape challenges the focus sharpening in the same frame. In the acquisition of the displacement field during the ultrasonic test, the focus has been set on the extremes of the specimen, where the highest displacements occur, while, for the strain acquisition in the pre-loading quasi-static cycle, the central portion, that corresponds to the most deformed region, has been focused. Nevertheless, regions proximal to the specimen extremities were properly focused thanks to the double curvature of the geometry, as shown in Fig. 5b.

The optimization problem has been therefore formulated as:

$$\min_{E_c} \sum \left| \frac{u^j_{exp,i} - u^j_{FEM,i}}{u^j_{exp,i}} \right| \tag{1}$$

such that:

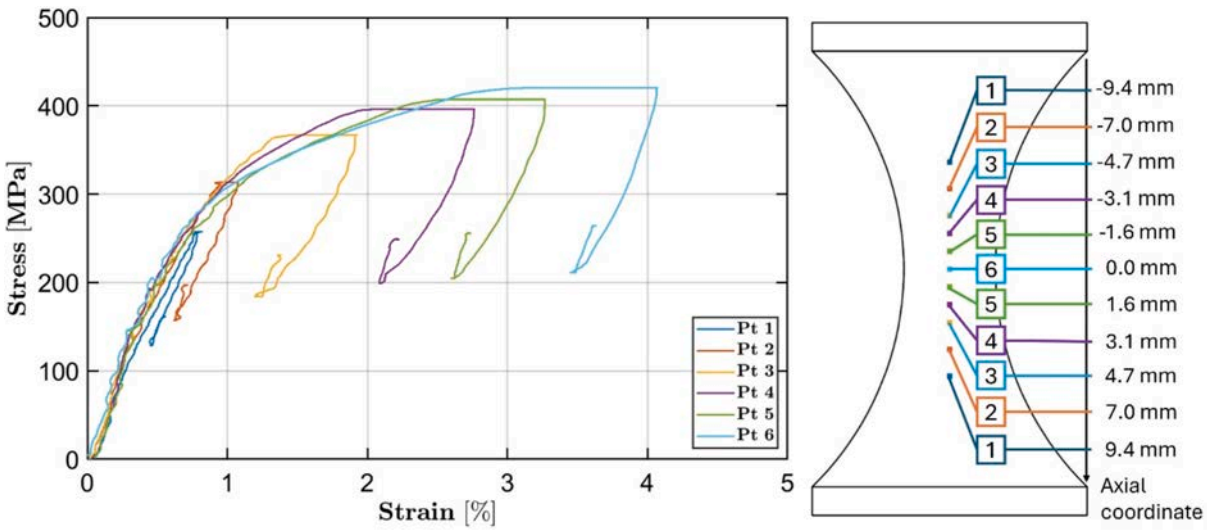

Fig. 7. Stress–strain curves along the specimen axis.

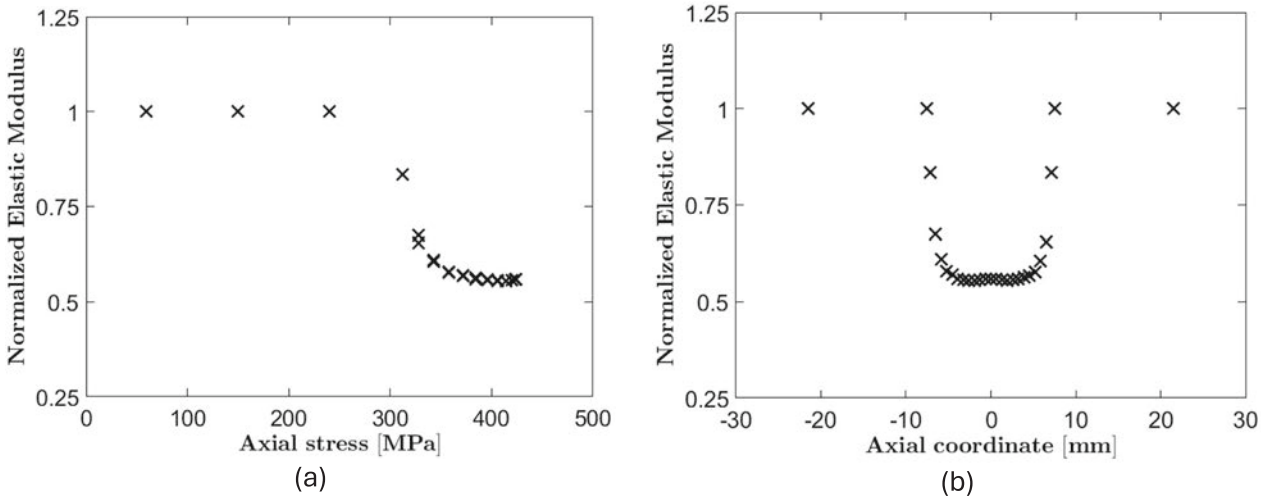

Fig. 8. Normalized Young' modulus variation: a) with the applied stress; b) along the specimen axis.

$E_c < 60GPa$

$19.5kHz < f < 20.5kHz$

where $u^j_{exp,i}$ and $u^j_{FEM,i}$ are the experimental and numerical displacements, respectively, at the i-th tracking point and j-th input voltage, E_c is the Young's modulus in the central portion of the specimen and f is the resonant frequency of the specimen.

4.1. Young's modulus variation with stress

Stress–strain curves at different locations along the specimen axis in the pre-loading cycle are represented in Fig. 7.

The same stress–strain response has been obtained in corresponding symmetrical points, as highlighted through the numbers. The nonlinear response occurs only in the central portion of the specimen, starting from point 2 of Fig. 7. Accordingly, the phase transformation is restricted to the central region of the specimen, while most of the specimen remains in the austenite phase. Moreover, results of Fig. 7 show the highly nonlinear behavior of the central cross-section of the specimen (Point 6) with the axial mean strain almost equal to 3.5 % at the end of pre-loading cycle. Finally, it is worth highlighting that, while holding the load at 210 MPa and 265 MPa, constant nonincreasing deformation is obtained. This confirms that the phase transformation has been fully achieved and that the martensite/austenite fraction remains stable.

The stress–strain curves allow to determine the Young's modulus variation with the applied stress and along the specimen axis, as represented in Fig. 8a and 8b.

Results are reported on a normalized scale, as the goal of this analysis was the determination of the Young's modulus variation with the applied stress (or along the specimen axis), while its amplitude will be determined in the ultrasonic loading conditions. The Young's modulus has been computed both in the unloading phase, when the load decreases from 420 MPa to 210 MPa, and in the loading phase, when the load is increased to 265 MPa. Limited variations have been obtained, and the average values have been retained.

According to Fig. 8a, the phase transition starts between 200 and 300 MPa, in accordance with the preliminary quasi-static test. Unlike the assumptions for the specimen design, the Young's modulus variation is not linear with the applied stress. As shown in Fig. 8b, the phase transformation is confined and affects a region 18 mm long. Moreover, for a length of 10 mm in the central region of the specimen, the austenite/martensite transformation fraction is constant.

In the FE model optimization, the variation of the Young's modulus along the specimen axis has been retained, as, given the limited stress amplitudes, no phase transformation occurs during the ultrasonic loading cycles. Accordingly, it is assumed that the Young's modulus equally varies along the specimen axis in the static and dynamic loading conditions. For the optimization problem, the experimental results reported in Fig. 8b have been interpolated with a third-order polynomial curve to guarantee the continuity of the Young's modulus along the specimen. Four conditions have been imposed for the identification of the parameters of the third-order polynomial, that are the Young's moduli and the two derivatives, imposed equal to zero, in the center of the specimen and in the extremes. At the extremes of the specimen, where only the austenite phase is present, the value of 60.0 GPa has been retained. Although vibrating at 20 kHz as the whole specimen, the strain amplitude in the extremities is limited or null. Accordingly, strain rate effects can be here neglected.

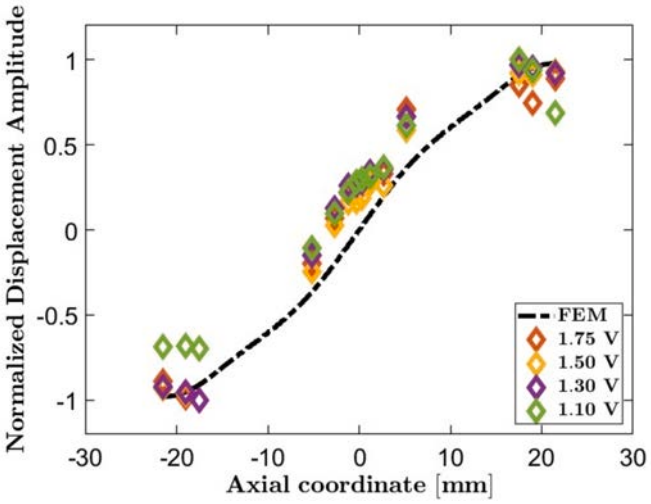

Fig. 9. Comparison of the experimental and numerical displacements of the optimized FE model.

4.2. FE model optimization

The optimization process has been performed in a Matlab subroutine with the zero-order Nelder-Mead algorithm [21]. At each iteration of the optimization process, the Young's modulus of the central region has been varied, and the third-order polynomial curve has been accordingly

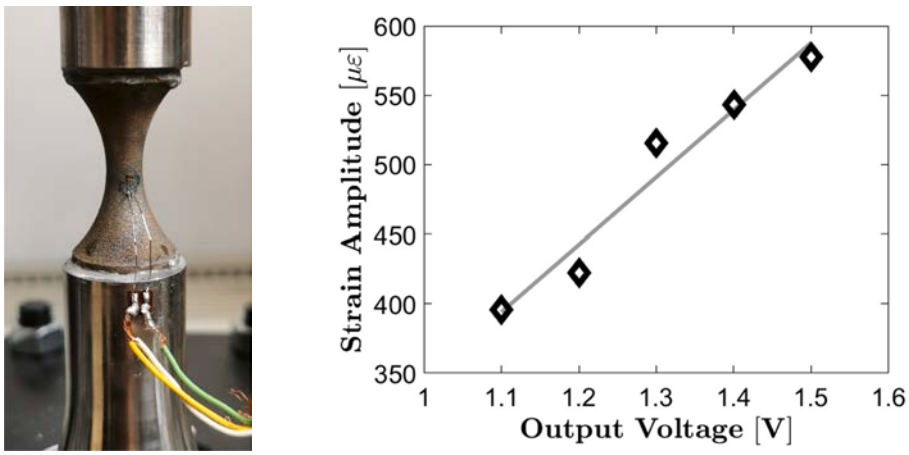

(a) (b)

Fig. 10. Strain gauge calibration: a) strain gage bonded at the specimen center to validate the applied strain amplitude during the ultrasonic fatigue tests; b) strain amplitude acquitted with the strain gage with respect to the voltage provided in output by the piezoelectric transducer.

reconstructed to guarantee the continuity of the Young's modulus along the specimen axis. The elastic constants of the FE model of Fig. 5a are then defined and the FE simulation can be performed. For comparing the experimental and numerical results, as the eigenvectors resulting from the modal analysis are known minus a constant, the numerical displacements have been normalized and multiplied by the experimental values acquired at the extremes for each input voltage.

Fig. 9 shows the comparison of the experimental and numerical displacements at different input voltages for the optimized FE model.

Results have been normalized with respect to the maximum displacement measured for each input voltage. The dynamic Young's modulus in the central region resulted equal to 48 GPa and accounts for the strain rate and cycling load effects [20]. With the dynamic Young's modulus and the assumed third-order polynomial curve variation along the specimen axis, a longitudinal resonant frequency of 20.0 kHz has been achieved.

4.3. Strain gauge calibration for the ultrasonic tests

The optimized FE model accurately captures the longitudinal displacement field and, accordingly, the strain field of the specimen and it is therefore adopted to compute the strain amplitude in the specimen center, once the relationship between the displacement amplitude at the specimen extremes and the input voltage provided to the piezoelectric transducer is known. However, to maximize the accuracy of the testing campaign, a strain gage validation has been carried out to assess the strain amplitude applied at the specimen center during the ultrasonic fatigue tests. Although the sampling frequency of high-speed camera allows to properly capture the displacement at the ultrasonic frequency, the reduced dimensions of the framed area challenge the strain computation from the acquired displacements. Accordingly, a micro-strain gage (HBM 1-LY11-0.3/120, with a grid length of 0.3 mm) has been bonded as close as possible to the specimen center, in a quarter bridge configuration. The Elsys SGA2-Box/7 system has been used to complete the Wheatstone bridge and amplify the voltage signal, acquired by a National Instrument DAQ device (NI USB-6361) with a sampling frequency of 300 kHz. The applied strain amplitude has been finally obtained through trigonometric interpolation. The input voltage has been varied between 1.1 V and 1.5 V. Higher voltages have not been considered to avoid temperature variations which could have influenced the strain measurement.

Fig. 10a shows the experimental setup for the validation of the applied strain amplitude, with the micro-strain gage bonded at the specimen center, while Fig. 10b plots the acquired strain amplitude with respect to the voltage provided in input by the piezoelectric transducer.

According to Fig. 10b, the experimental strain amplitude follows a linear trend, as expected. This strain gage validation provides an accurate assessment of the applied strain amplitude during the VHCF tests. From this experimental relationship, the applied stress amplitude can be accurately assessed, by considering the Young's modulus distribution obtained with the optimization procedure based on the high-speed camera acquisitions.

5. Results

5.1. Defects analysis by μ-CT

To observe internal defects present in the specimens and to evaluate their influence on the measured results, an x-ray micro-Computed Tomography (μ-CT) scanner has been employed. The scanner available within the J-Tech@PoliTO research facilities was designed and built by Fraunhofer Institute, having a 300 kV conic x-ray source, with a nominal focal spot of 3 μm, paired with a 2048 × 2048 pixels flat panel detector. For the scan, the specimens have been placed on a stage between the source and the detector, and 1600 x-ray projections have been acquired at constant angle steps from 0° to 360°, being the same machine and similar configuration as the one used in [22].

The optimal settings for these analyses comprised a voltage of 270 kV and a current of 130 μA on the tungsten filament of the source. A distance between the source and the detector of 700 mm, and 52.5 mm between the source and the stage's axis of rotation have been set, amounting to a scanning resolution of 15 μm. Additionally, a tin (Sn) filter has been used, with a thickness of 2.4 mm, aiming to minimize the beam hardening phenomenon, by blocking low-energy x-rays.

The 2D projections acquired during the CT scan have been then used to reconstruct the 3D digital image of the specimen, with software from Volume Graphics, VGSTUDIO MAX 3.5. The software also allowed the internal defects of the specimen to be identified through the porosity/inclusion analysis module.

This module algorithm operates by identifying whether each voxel belongs to a defect by forming clusters of connected voxels. These clusters are then assessed to determine if they meet the user-defined analysis criteria. In this study, the VGDefX algorithm is utilized for its ability to accurately detect imperfections, even in noisy regions or those linked to surrounding air near the specimen's surface. Additionally, this algorithm enables the inclusion of various probability criteria to enhance defect detection, including the possibility of uniting defects that are too close to each other, essentially producing one large defect. In this case, if the gap between the borders of two defects is equal inferior to four voxels, the algorithm evaluates the possibility of uniting them

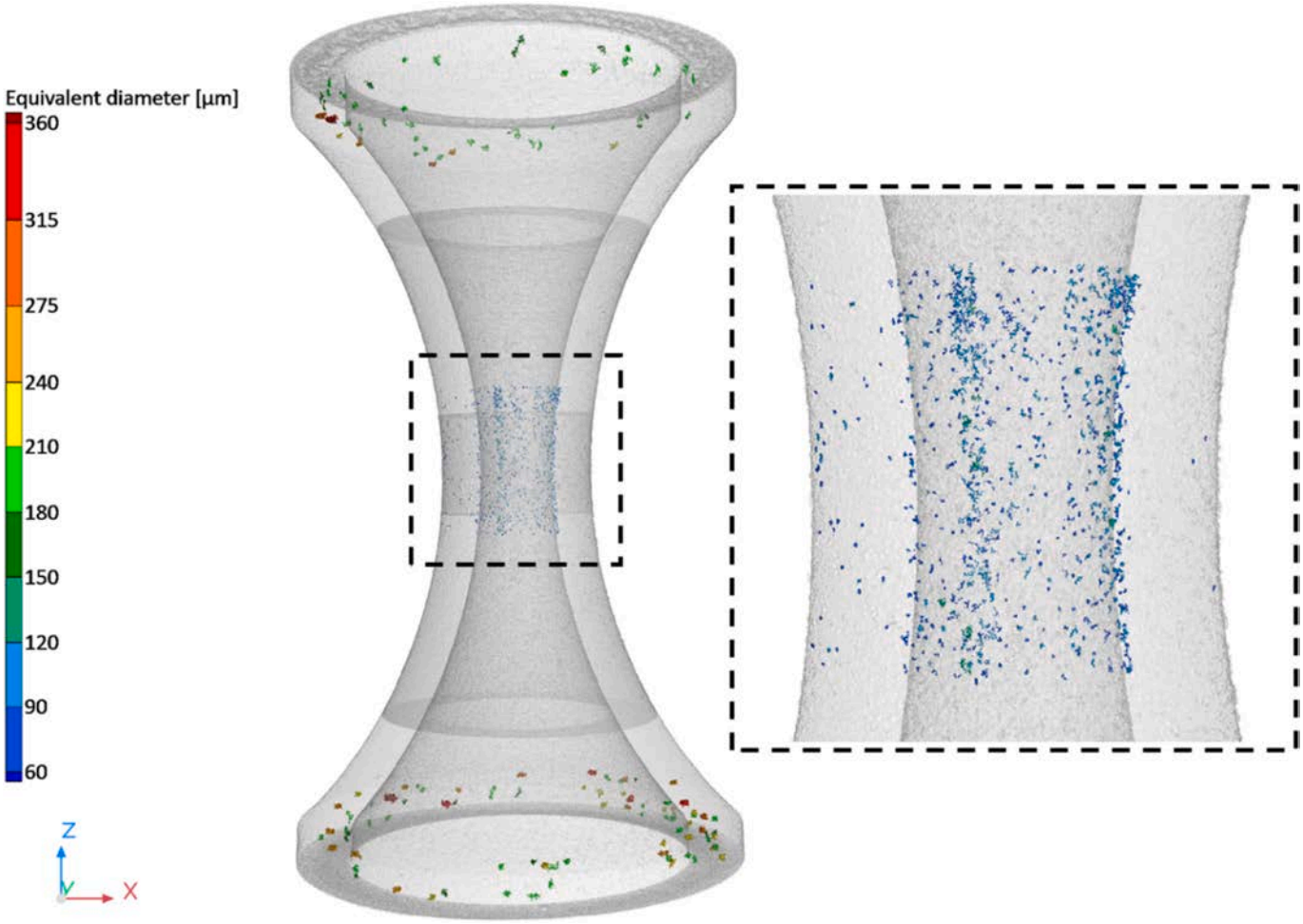

Fig. 11. Characteristic defect distribution comparing the largest defects in the center and in the extremities of the specimen.

depending on the gray levels of the gap and the contour gradient of the two defects.

μ-CT scans have been performed on several specimens before the fatigue tests, to assess the defect population. Fig. 11 shows the typical defect populations observed in the scanned specimens, expressed in terms of equivalent diameter, i.e., the diameter of a sphere with the same volume as the defect.

The detectable defects in CT scanning correspond to those with a length, in any direction, of at least four times the resolution, in this case 60 μm, as established by previous works on CT scanning statistical data analysis [23–25]. The different color tones in the 3D shape of the specimen correspond to the overlap between the scanned parts of the specimen, which has been scanned three times (top extremity, bottom extremity and center), so as to maximize the resolution.

Fig. 11 compares the defects identified at the center of the specimen with the largest defects at the extremities, corresponding to those of at least 150 μm of equivalent diameter, highlighting the general larger size of the latter. The smaller defects of the extremities are hidden to facilitate visualization, while all defects detectable at the center are shown. The different sizes of defects in the center and in the extremes can be attributed to geometrical features and manufacturing parameters. Optimal parameters for the printing process were identified in [16] on small cubic specimens with the aim of maximizing the relative density. However, as the specimen diameter increases, time between laser fusions of two consecutive layers also increases and heat transfer increasingly plays a key role. The central part of the sample exhibited small pores, which can be also found typically in the highest density condition [16] and appears as gas pores. On the contrary, the bottom and the top regions of the samples have larger defects, which are recognized as lack of fusion defects, as in these regions heat transfer is facilitated.

Fig. 12 instead shows the defect population of a peculiar specimen, which represented an outlier as concerns defectiveness.

It can be noticed that the population of the defects in the center of the specimen in Fig. 12 is smaller both in quantity and dimension when compared to the average defect population assessed in other specimens and reported in Fig. 11. On the contrary, a similar population of defects above 150 μm of equivalent diameter can be observed in the extremities.

Table 3 reports the largest defect in the extremity and in the center for the specimens in the average (Fig. 11) and outlier (Fig. 12) specimens. Specifically, the values for the equivalent diameter and the projected sizes of the defect in each cartesian axis are reported.

While comparable largest sizes have been observed at the extremes, the outlier specimen is characterized by a consistently smaller defect in the center. The limited defect population of the outlier specimen resulted in outperforming fatigue results, as will be shown in Section 5.2.

It is important to highlight that the specimen referred to as an outlier was manufactured according to the same procedure as the other specimens, being an outlier due to the significantly different defect population encountered in its central region. As a total of 6 specimens were CT-scanned, including the outlier, to further demonstrate these differences, Table 4 is added, reporting the range of equivalent diameters and number of defects found in each of the 5 specimens considered “average” and for the outlier specimen.

Indeed, Table 4 shows how both the number of defects and range of

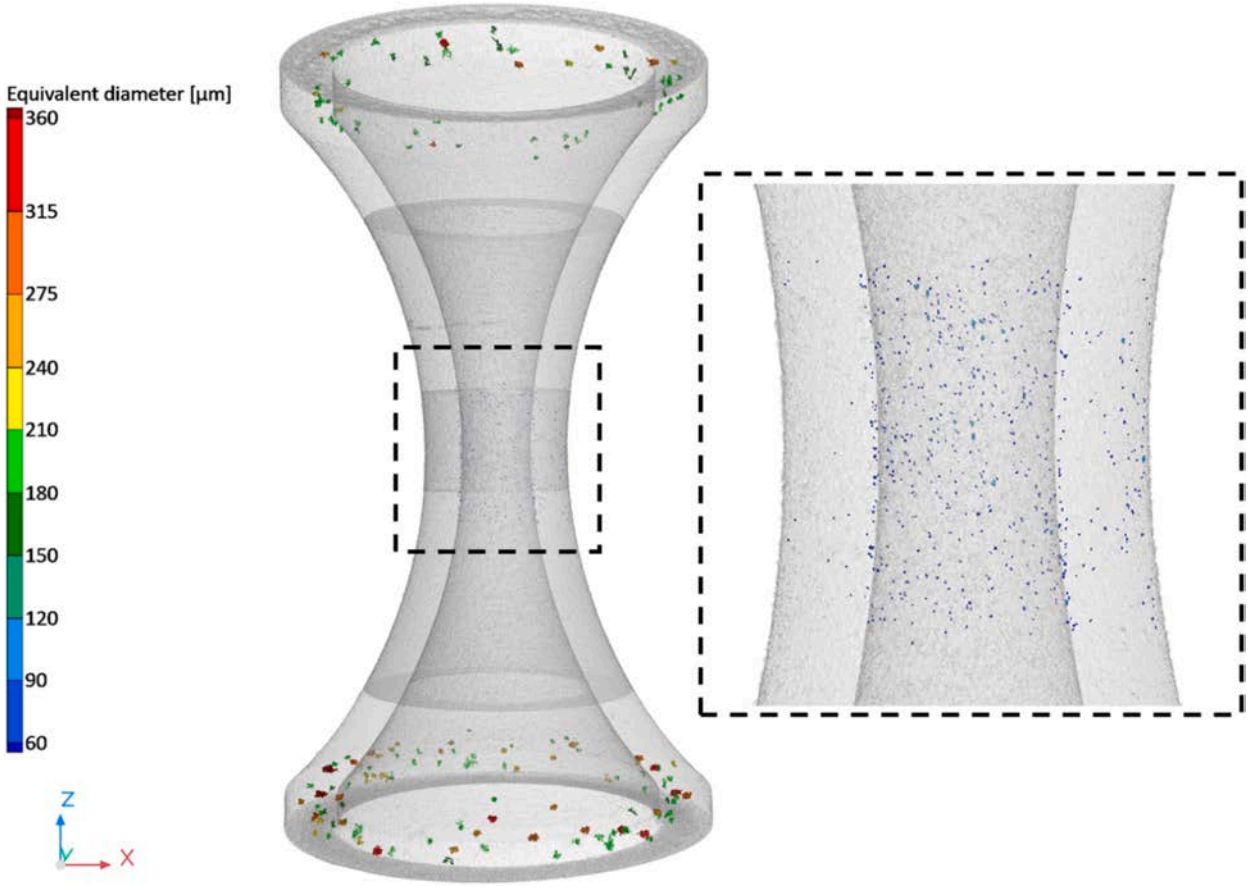

Fig. 12. Defect distribution comparing the largest defects in the center and in the extremities of the specimen representing an outlier as characterized by a consistently smaller defect population in the central region.

Table 3
Average material properties determined through the conducted tests.

Specimen	Defect position	Equivalent diameter [µm]	Projected size x [µm]	Projected size y [µm]	Projected size z [µm]
Average specimen	Center	133	330	195	338
(Fig. 11)	Extremity	360	728	704	496
Outlier specimen	Center	100	150	150	120
(Fig. 12)	Extremity	347	624	640	400

Table 4
Comparison of defect analysis results for the outlier specimen with the remainder of the scanned specimens.

Specimen group	Equivalent diameter range [µm]	Total number of identified defects
Outlier specimen	67–100	157
All scanned specimens excluding the outlier	67–140	618–851

sizes are smaller at the center of the outlier specimen. The minimum range of equivalent diameter of 67 µm is a consequence to the imposition of at least 60 µm of length in any direction for the detected defects, as previously explained.

To further illustrate the differences between the defect population near the center of the outlier specimen and the 5 other CT-scanned specimens, Fig. 13 represents the equivalent diameter of the defects with respect to the sphericity.

A low sphericity of a defect – given by the ratio between the surface of a defect and the smallest sphere that could contain that defect – is often correlated to a larger defect size, with both characteristics being responsible for an increase in the stress concentration [26]. This highlights a further discrepancy between the outlier specimen and the other specimens, which reflects on the fatigue response, as will be shown in the next section.

5.2. Results of the fatigue tests

The geometrical features of the hourglass specimen determine axial, circumferential and radial stresses. In the following, the results of the fatigue tests are therefore reported in terms of equivalent stress amplitude, computed with the Von Mises criterion [27]. The trend between the applied equivalent stress with respect to the number of cycles to failure has been estimated by applying the Least Square Method. To model the experimental variability and estimate the S-N curves at different reliability levels (Probabilistic-S-N curves), the logarithm of the fatigue life has been assumed to be Normally distributed, with the mean of the distribution linearly dependent on the logarithm of the equivalent stress (according to the Basquin power law) and constant standard deviation. Due to the large number of runout data and the large variability of fatigue life (i.e., for the same equivalent stress, specimens

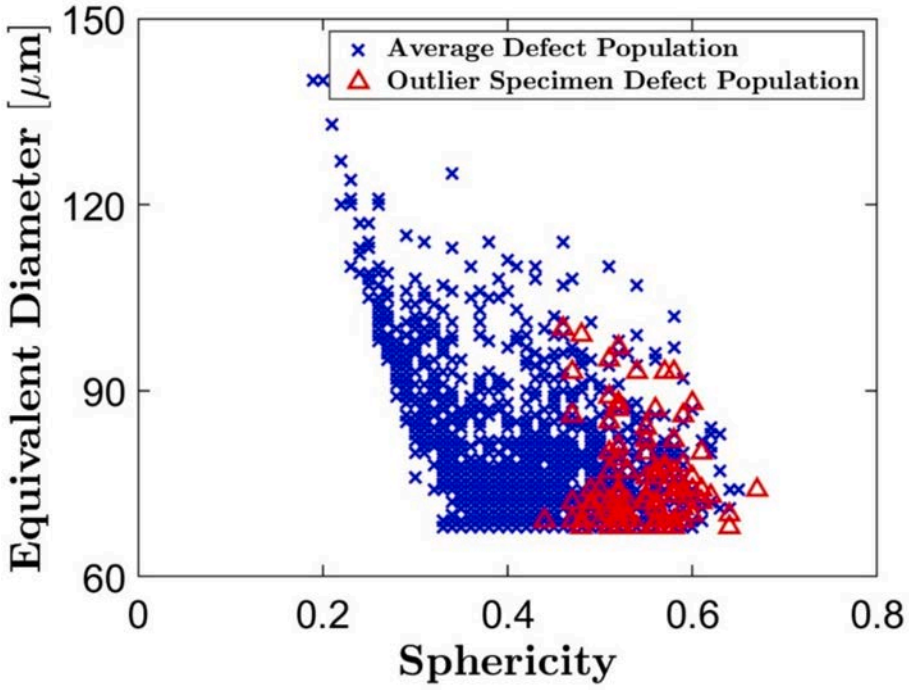

Fig. 13. Equivalent diameter with respect to sphericity of the entire identified population of defects near the center of the specimens.

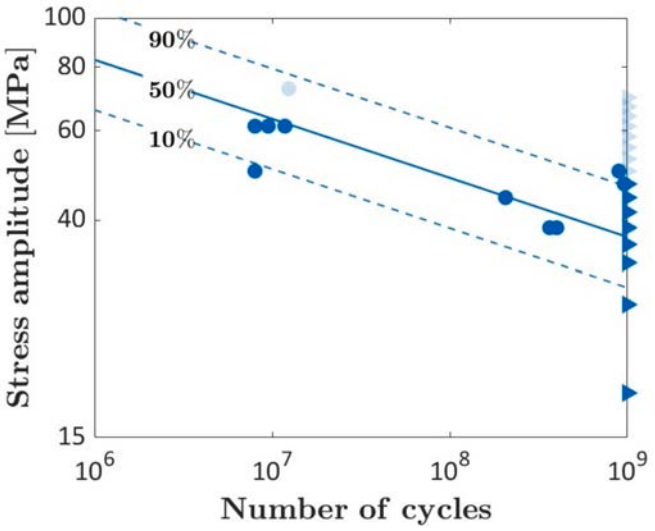

Fig. 14. Experimental data and median, 0.1-th and 0.9-th P-S-N curves on the S-N plot for the tested Nitinol alloy. (transparent markers refer to the low defective specimen not considered for the estimation of the P-S-N curves).

failing close to 10^7 cycles and runout data have been found), methodologies allowing to account also for runout data have not been conservatively considered, to properly model the trend of failure data.

Fig. 14 plots the experimental data in an S-N plot, together with the median, the 10-th and 90-th quantile P-S-N curves.

Transparent markers have been used for the experimental data obtained by testing the specimen with limited defectiveness analyzed in Section 5.1 (see Fig. 12).

According to Figs. 14, 10 failures and 16 runout data have been experimentally obtained, with number of cycles to failure ranging between $8 \bullet 10^6$ and $9.59 \bullet 10^8$. The applied equivalent stress ranged between 18 MPa and 73 MPa, with no failures below 39 MPa. According to Fig. 14, the assumed linear decreasing trend can be considered appropriate for fitting experimental data, with an asymptotic trend, corresponding to a possible fatigue limit, not evident for very high number of cycles close to 10^9 cycles. The experimental scatter is quite large and about 67 % of the experimental data falls between the 0.9-th and 0.1-th P-S-N curves. In particular, one failure is below the 0.1-th quantile P-S-N curve, pointing out that higher reliability percentile curves are to be considered for a safe design and to properly account for the large experimental scatter. It must be also noted that the variability of equivalent stress associated with runout data is quite large, with an equivalent stress amplitude ranging from 18 MPa to 70 MPa. However, runout data at stresses comprised between 50 MPa and 70 MPa (transparent triangle markers) have been obtained with the specimen analyzed in Section 5.1 and characterized by a consistently low defectiveness, especially in the central most loaded region. The characteristic defect population of the specimen, that, according to Fig. 13, contains smaller and more spherical defects than those identified in the other specimens, determines outperforming fatigue performance, that has not been conservatively considered for the estimation of the P-S-N curves.

These analyses and, mainly, the large variability associated with the runout data, point out the significant influence of material defectiveness on the resulting fatigue response, as will be discussed in Section 6, with the absence of large defects allowing for prolonged fatigue life.

6. Discussion

Fig. 15 shows the typical failure mode, with the crack longitudinally propagating along the specimen axis, as result of the axial and circumferential stresses.

The results of the μ-CT scans have shown that the defect population in the specimen center governs the fatigue response. Indeed, the outlier specimen has shown an outperforming fatigue response compared to the other specimens, as result of the limited defect population in the central region. On the contrary, as observed in Section 5.1, the defect populations in the average and outlier specimens were similar in the extremity. Accordingly, the crack started from defects in the specimen center, where the highest axial and circumferential stresses acted, and propagated towards one of the specimen extremities.

To prove this, FE analyses have been performed on Representative

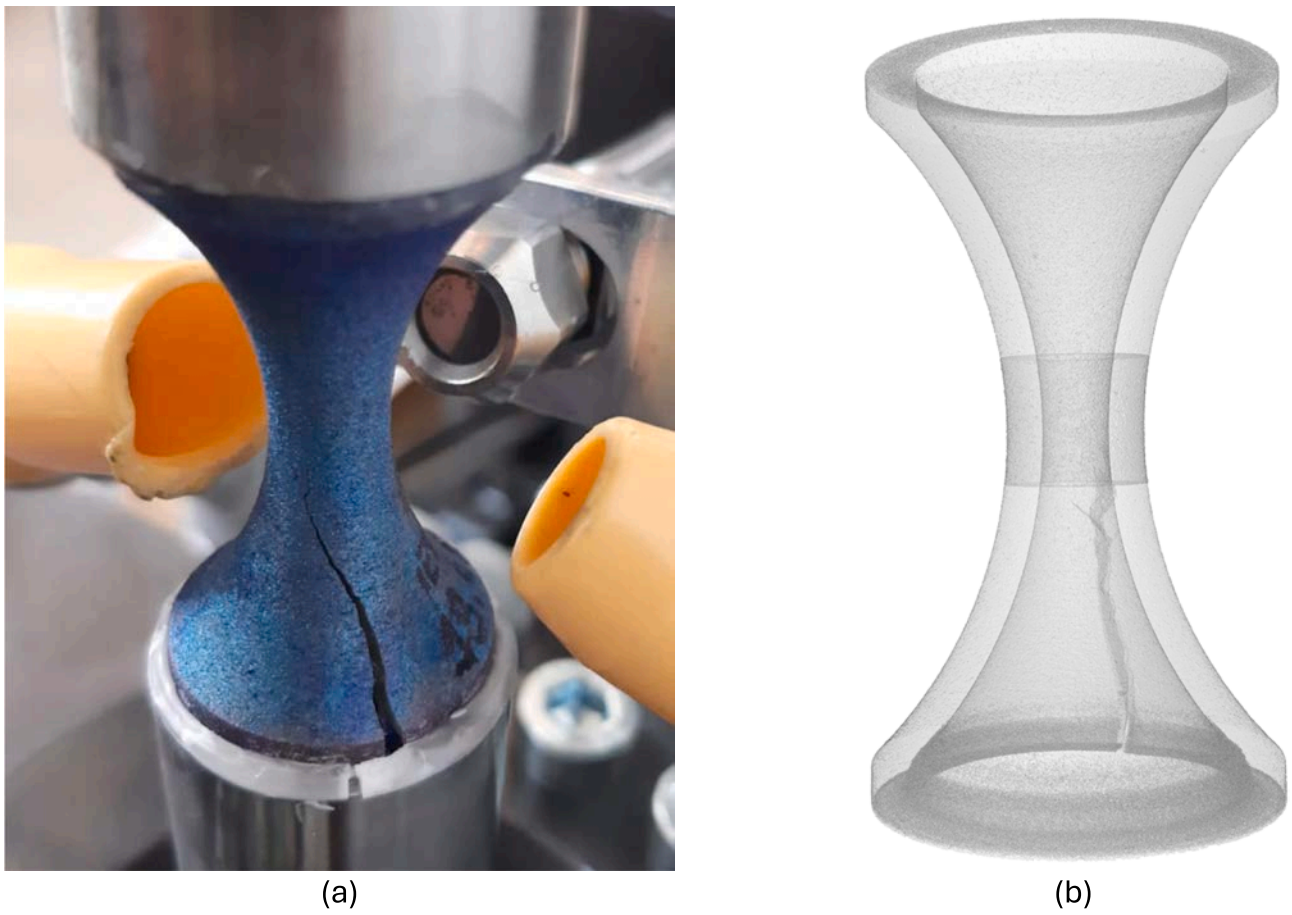

Fig. 15. Failure mode of the tested specimen due to the axial and circumferential stresses: a) cracked specimen; b) μ-CT reconstruction.

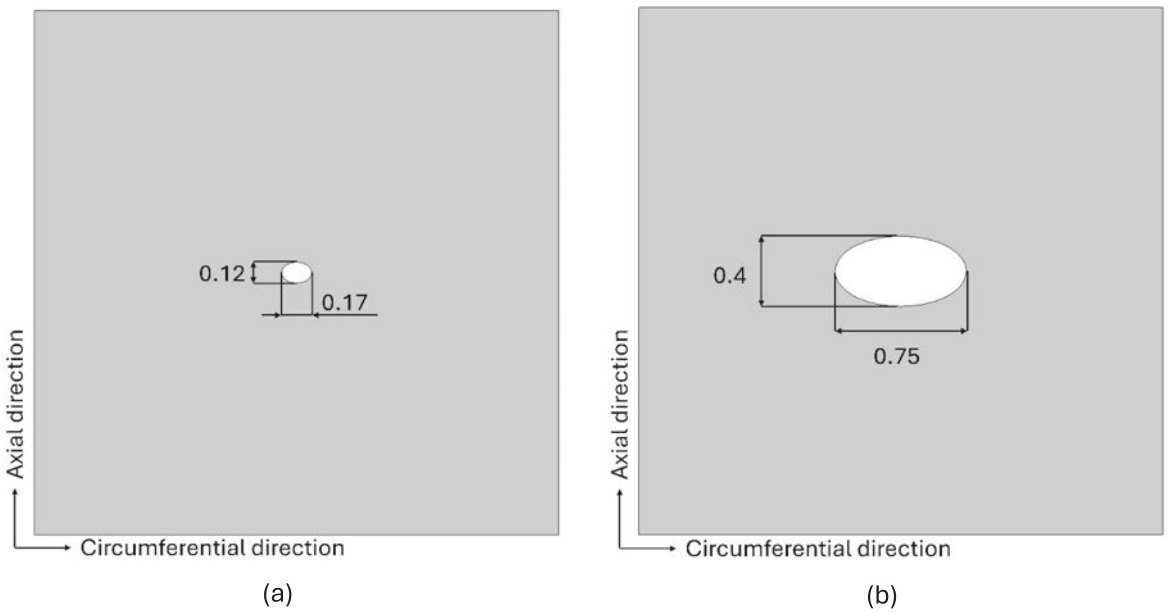

Fig. 16. RVEs for the investigation of the stress field surrounding a defect: a) typical defect size in the specimen center; b) typical defect size in the specimen extremities. Dimensions are in mm.

Volume Elements (RVEs) by investigating the stress field surrounding a defect. In particular, the comparison has retained the stress fields surrounding the largest defects identified with the μ-CT scans in the center and in the extremity of the outperforming specimen (see Table 3). Despite the thin cross-section, the double curvature of the hourglass geometry determines both circumferential and radial stresses. However, in the specimen center, the geometry bends only around the specimen axis and the radial stresses are null. Accordingly, the specimen

Table 5
Material properties retained in the shape memory material model.

Property [Unit]	Value
$S_{A-M,i}$ [MPa]	210.0
$S_{A-M,u}$ [MPa]	450.0
$S_{M-A,i}$ [MPa]	125.0
$S_{M-A,u}$ [MPa]	115.0
ε_{Mr} [-]	0.028

experiences a biaxial stress condition due to axial and circumferential stresses. Given the plane stress condition in the specimen center and extremes, the analysis has been performed by means of 2D shell elements. Although the stress field surrounding a defect can be accurately captured only by considering its actual shape, the goal of this analysis is to prove the higher criticality of central pores over those at the extremes of the specimen. Accordingly, an equivalent shape has been retained, with the defect modelled as an ellipse, where the first semiaxis is the projection of the defect size along the specimen axis and the second is the projection of the defect size along the circumferential direction, thus capturing the characteristic defect sizes that influence the mechanical response. Through simple geometrical considerations, the second semiaxis can be computed from the projections along the two axes perpendicular to the specimen axis and from the information on the defect radial position. For the defect in the specimen center, the semiaxes resulted equal to 120 μm and 170 μm along the axial and circumferential directions, respectively. The defect in the specimen extremities was 400 μm by 750 μm along the axial and circumferential directions, respectively.

Fig. 16 show the RVEs for the investigation of the stress field in correspondence of the defects.

The size of the RVEs as well as the shell elements mesh size have been identified by means of a convergence analysis, resulting equal to 3x3 mm and to 0.01 mm, respectively. The investigation of the local stress field must account for the strongly nonlinear response of the Nitinol alloy in the pre-loading cycle. Shape memory material behavior has been considered, whose properties [28] have been determined through a trial-and-error process aiming at replicating the stress–strain curves assessed along the specimen axis, shown in Fig. 7. Table 5 reports the identified material properties, i.e., the stress levels at which the conversion of austenite into martensite begins, namely $S_{A-M,i}$, and is completed, namely $S_{A-M,u}$, the stress levels at which the reverse transformation of martensite into austenite begins, namely $S_{M-A,i}$, and is completed, namely $S_{M-A,u}$, and the residual strain if the material is unloaded in the martensite phase, namely ε_{Mr}, which defines the size of the hysteresis cycle of the material.

Moreover, the Young's modulus of the martensite phase has been imposed equal to 20 GPa, as determined in the quasi-static pre-loading cycle.

On the upper and bottom nodes of the RVE model, the axial stress history of the pre-loading cycle has been applied. The left and right nodes have been instead subjected to the circumferential stress history

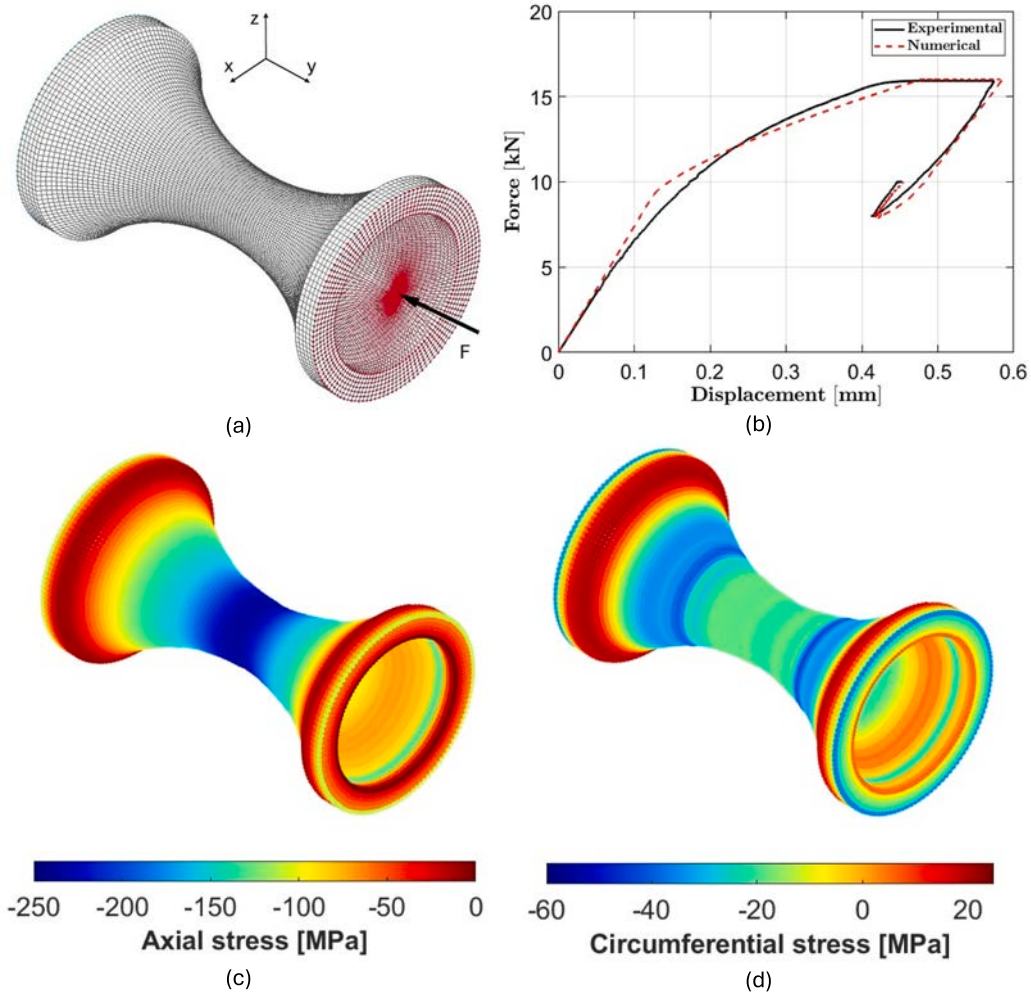

Fig. 17. FE simulation of the specimen with shape memory material model: a) FE model b) comparison of experimental and numerical force–displacement curves; c) contour plot of the axial stress distribution; d) contour plot of the circumferential stress distribution.

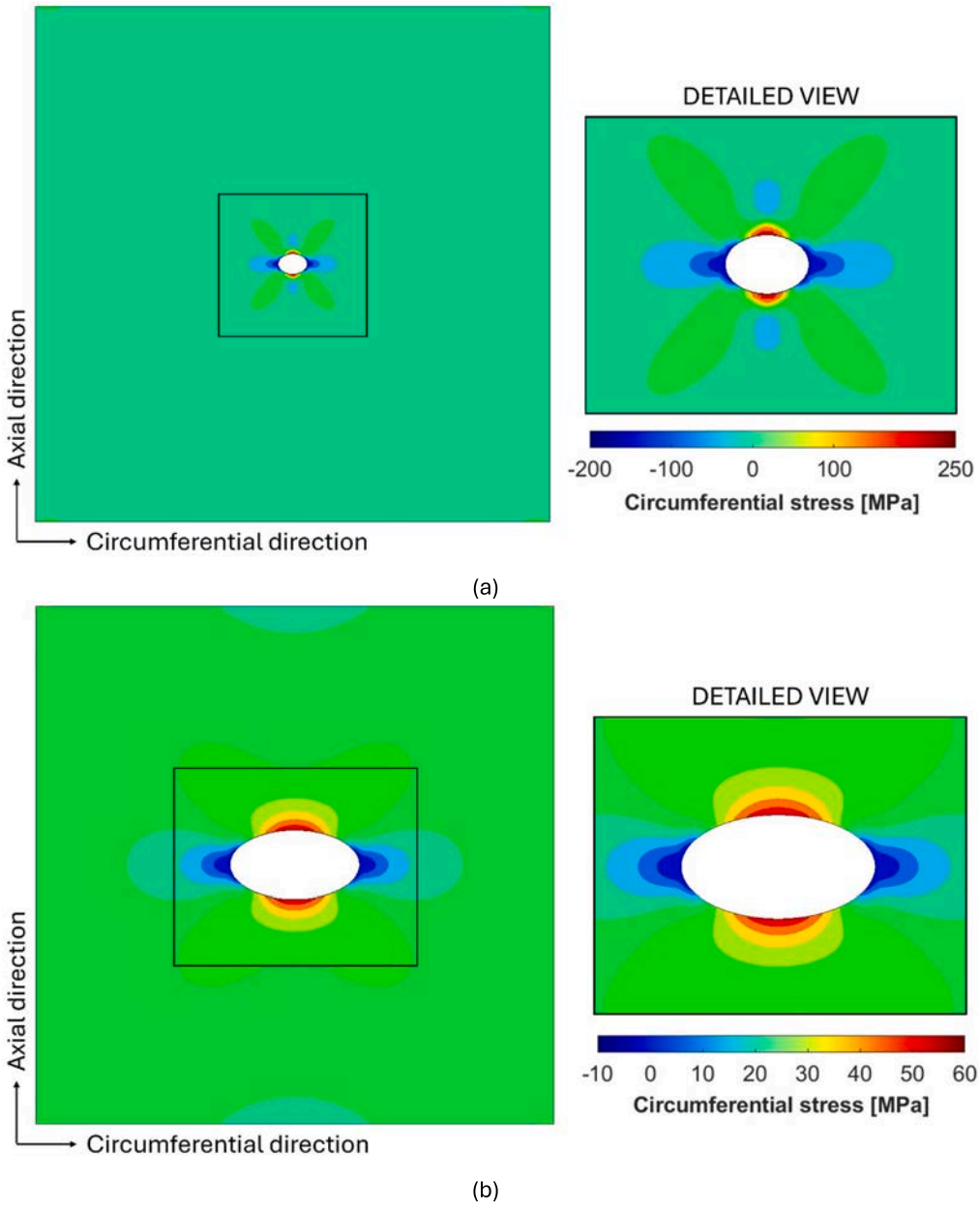

Fig. 18. Stress field surrounding internal defects: a) defect in the specimen center; b) defect on the outer surface of the specimen extremity; c) defect on the inner surface of the specimen extremity.

of the pre-loading cycle. The axial and circumferential stress histories have been determined through a FE analysis of the whole specimen, where the same shape memory material model has been retained. The FE model of the whole specimen adopted 3D hexagon solid elements, with a mesh size of 0.5 mm. To replicate the constraining influence of the upper and bottom horns, the upper and lower nodes have been rigidly connected to a central master node with RBE2 elements. The bottom central node has been fully constrained while the upper node has been loaded in accordance with the pre-loading cycle. Given the nonlinear material response, the FE analyses of the RVEs and of the whole specimen have been performed with explicit time integration adopting a time-scaling approach to reduce the computational time. The material model indeed does not consider strain rate effects, as the model aims at simulating the pre-loading quasi-static cycle. Moreover, the application of a mass-scaling approach can consistently alter the results, as the loading cycle is performed in the force-controlled configuration.

Fig. 17a and 17b report the FE model of the whole specimen with shape memory material model and a comparison of the experimental and numerical force–displacement curves for validation, respectively. Moreover, Fig. 17c and 17d represent the resulting axial and circumferential stress contour plots.

As shown in Fig. 17, only the extremities of the specimen are subjected to a macroscopic tensile stress in the circumferential direction. In the specimen center, both the axial and the circumferential stresses are compressive. The loading histories of the most loaded elements in the center and in the extremity of the specimen have been retained for the RVE analyses. For the center of the specimen, it has been found that, at the end of the pre-loading cycle, the axial compressive stress is 265 MPa and the circumferential compressive stress is 35 MPa. For the specimen extremity, on the outer surface, the material is compressed along the axial direction by 10 MPa and tensioned along the circumferential direction by 22 MPa. On the inner surface of the specimen extremity,

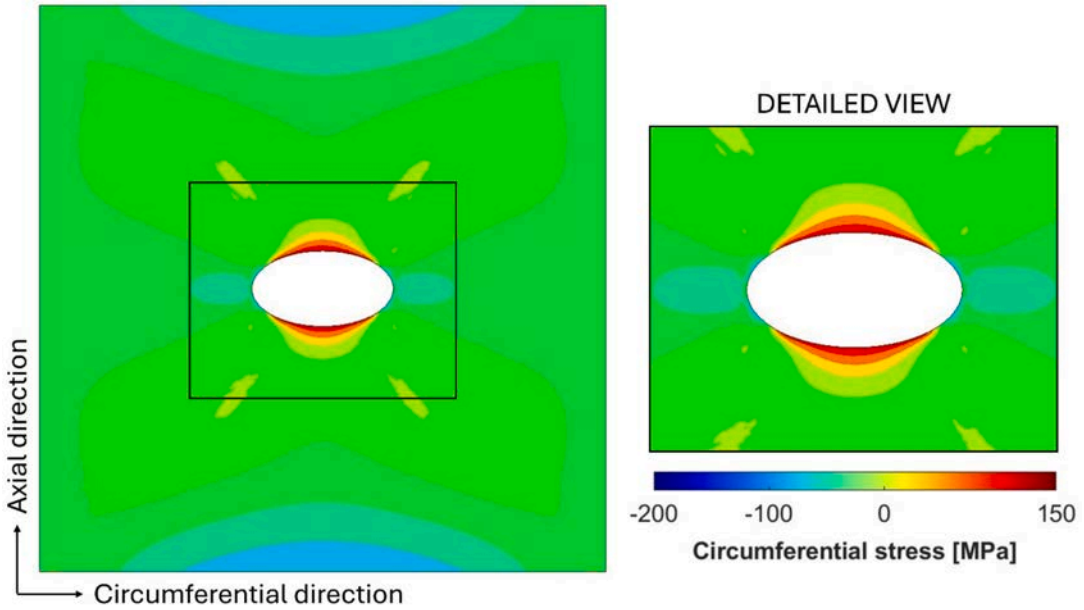

(c)

Fig. 18. (*continued*).

instead, the FE analysis shows that the material is compressed along both the axial and circumferential directions by 140 MPa and 30 MPa, respectively.

Fig. 18 reports the circumferential stress fields of the RVE simulations. Fig. 18a reports results for the defect in the specimen center, while Fig. 18b and Fig. 18c show the circumferential stress fields surrounding a defect in the specimen extremity on the outer and inner surfaces, respectively.

The RVE analysis shows that, although the specimen center is macroscopically compressed along both the axial and circumferential directions, tensile stresses arise along the circumferential direction in correspondence of internal defects. Such tensile circumferential stresses in the specimen center are responsible for the crack propagation along the specimen axis observed in the tested specimens (see Fig. 15). Indeed, despite the significant difference in the defect sizes, the comparison clearly shows the highest criticality of the stress field surrounding a defect in the specimen center, where the average circumferential stress is almost equal to 220 MPa, while on the outer and inner surfaces of the specimen extremity, it is equal to 60 MPa and 130 MPa, respectively. In addition to the higher tensile average stress along the circumferential direction, the specimen center experiences the highest alternate stresses, which instead tend to zero at the extremities. It is worth remarking that the aspect ratio of the ellipsoidal defect shape here plays a limited role in enhancing circumferential stresses, which are mainly governed by the remote axial component.

Combining the alternate and average stresses with the Smith-Watson-Topper criterion, a Stress Intensity Factor (SIF) can be computed for the defects in the center and in the extremity. According to the Smith-Watson-Topper criterion, SIF can be computed as

$$SIF = 0.5 \bullet \sigma_{eq} \bullet \sqrt{\pi \bullet a} \tag{1}$$

being σ_{eq} the equivalent stress computed, in accordance with the Smith-Watson-Topper criterion, as $\sqrt{\sigma_a \bullet \sigma_m}$, where σ_a and σ_m are the alternate and average stress components, respectively, and a is the defect size along the axial direction. The reduction of the SIF from the specimen center to the specimen extremity is about 64 % and 50 %, for the outer and inner surfaces, respectively, further confirming the higher criticality of defects in the center of the specimen with respect to those in the specimen extremities. The RVE analysis moreover demonstrates that the longitudinal crack propagation is caused by local tensile stresses that arise around defects. It is worth highlighting that the defect size is not the unique parameter affecting the fatigue performance: the numerosity of defects, influencing the reciprocal interactions, and the proximity to the specimen surface are indeed important factors that can also affect the fatigue response (see Figs. 10 and 11). Moreover, it is worth remarking that the aim of this analysis is to provide a qualitative demonstration of the observed crack path, as quantitative information can be captured only through 3D solid elements, which account for the triaxial stress state in correspondence of the defect. Also, the actual shape of the scanned defects should be used to quantitatively assess the stress field surrounding the defect, as the defect shape, such as its sphericity, influences the stress increase in correspondence of the defect. Finally, the mutual influence of proximal defects and of the surface roughness can play an important role in the fatigue response of the material.

7. Conclusions

This paper investigates the Very High Cycle Fatigue (VHCF) response of an Additively Manufactured (AM) Nitinol alloy by means of the ultrasonic fatigue testing technique. To resemble in-service loading conditions of typical Nitinol components, such as heart stents, the ultrasonic cyclic loading is applied to the partially transformed material, which is induced by compressing the material through an electrodynamic machine. An innovative experimental setup has been proposed, where the martensite/austenite transformation fraction is controlled, and the partially transformed material is fatigued up to 10^9 cycles.

The peculiar characteristics of the Nitinol alloy in the phase transition region challenge the standard methods for designing specimens for ultrasonic tests. An iterative Finite Element (FE) procedure has been here adopted to define an hourglass-shaped hollow specimen, which assumes a linear variation of the material Young's modulus with the applied stress starting from 200 MPa, i.e., the stress starting value for the forward phase transformation (conversion of austenite into martensite). The FE model has been also optimized on the displacement field acquired with a high-speed camera during the ultrasonic test, thus allowing the accurate characterization of the dynamic Young's modulus

of the partially transformed material, i.e., the elastic modulus in the dynamic loading conditions, and a reliable computation of the stress amplitude.

Results of the VHCF tests and μ-CT scans show that material defectivity plays a key role in the fatigue performance and failure mode of the tested specimens. Although subjected to a biaxial compressive plane stress state in the longitudinal and circumferential directions, local tensile stresses arise in the circumferential direction in correspondence of defects, as shown through FE analyses on Representative Volume Elements (RVEs) of scanned defect sizes, determining a longitudinal crack propagation. Moreover, consistently smaller defects were found at the center of the specimen showing prolonged fatigue life and with the highest runout stress amplitude, thus confirming the influence of defects on the investigated VHCF response. In the VHCF tests, failures have been obtained for number of cycles ranging between $8 \bullet 10^6$ and $9.6 \bullet 10^8$ and applied equivalent stress comprised between 39.0 MPa and 73 MPa. Fatigue results have not evidenced an asymptotic trend, corresponding to a possible fatigue limit of the material.

CRediT authorship contribution statement

C. Boursier Niutta: Writing – original draft, Validation, Methodology, Formal analysis, Data curation, Conceptualization. **A.P. Pagnoncelli:** Data curation, Conceptualization, Visualization, Methodology, Investigation. **A. Tridello:** Software, Methodology, Conceptualization, Writing – review & editing, Supervision. **J. Fiocchi:** Writing – review & editing, Investigation. **C.A. Biffi:** Writing – review & editing, Investigation. **A. Tuissi:** Writing – review & editing, Supervision, Resources, Funding acquisition. **D.S. Paolino:** Resources, Supervision, Project administration, Funding acquisition, Conceptualization, Writing – review & editing.

Declaration of competing interest

The authors declare that they have no known competing financial interests or personal relationships that could have appeared to influence the work reported in this paper.

Acknowledgments

This work has been supported by the Research Project MICS funded by the Italian Ministry of University and Research.

Data availability

Data will be made available on request.

References

[1] Mohd Jani J, Leary M, Subic A, Gibson MA. A review of shape memory alloy research, applications and opportunities. Mater Des 2014;56:1078–113. https://doi.org/10.1016/j.matdes.2013.11.084.
[2] Senthilnathan K, Shamimi A, Bonsignore C, Paranjape H, Duerig T. Effect of prestrain on the fatigue life of superelastic nitinol. J Mater Eng Perform 2019;28:5946–58. https://doi.org/10.1007/s11665-019-04334-2.
[3] Otsuka K, Ren X. Physical metallurgy of Ti-Ni-based shape memory alloys. Prog Mater Sci 2005;50:511–678. https://doi.org/10.1016/j.pmatsci.2004.10.001.
[4] Mehrpouya M, Alberto Biffi C, Lemke JN, Bregoli C, Fiocchi J, Mohajerani S, et al. Additive manufacturing of architected shape memory alloys: a review. Virtual Phys Prototyp 2024;19. https://doi.org/10.1080/17452759.2024.2414395.
[5] Elahinia M, Shayesteh Moghaddam N, Taheri Andani M, Amerinatanzi A, Bimber BA, Hamilton RF. Fabrication of NiTi through additive manufacturing: a review. Prog Mater Sci 2016;83:630–63. https://doi.org/10.1016/j.pmatsci.2016.08.001.
[6] Hou J, Wei C, Wang J, Gu X, Zhu J, Zhang W. Topology optimization for energy dissipation structures based on shape memory alloys. Struct Multidiscip Optim 2023;66. https://doi.org/10.1007/s00158-023-03491-2.
[7] Liu X, Gu D, Yuan L, Shi X, Shi K, Sun J, et al. Topological optimisation and laser additive manufacturing of force-direction-sensitive NiTi porous structures with large deformation recovery behaviour. Virtual Phys Prototyp 2024;19. https://doi.org/10.1080/17452759.2024.2365860.
[8] Chowdhury S, Yadaiah N, Prakash C, Ramakrishna S, Dixit S, Gupta LR, et al. Laser powder bed fusion: a state-of-the-art review of the technology, materials, properties & defects, and numerical modelling. J Mater Res Technol 2022;20:2109–72. https://doi.org/10.1016/J.JMRT.2022.07.121.
[9] Weaver JD, Sena GM, Aycock KI, Roiko A, Falk WM, Sivan S, et al. Rotary bend fatigue of nitinol to one billion cycles. Shape Mem Superelasticity 2023. https://doi.org/10.1007/s40830-022-00409-7.
[10] Robertson SW, Pelton AR, Ritchie RO. Mechanical fatigue and fracture of Nitinol. Int Mater Rev 2012;57:1–36. https://doi.org/10.1179/1743280411Y.0000000009.
[11] Berti F, Spagnoli A, Petrini L. A numerical investigation on multiaxial fatigue assessment of Nitinol peripheral endovascular devices with emphasis on load non-proportionality effects. Eng Fract Mech 2019;216. https://doi.org/10.1016/j.engfracmech.2019.106512.
[12] Fitzka M, Rennhofer H, Catoor D, Reiterer M, Lichtenegger H, Checchia S, et al. High speed In situ synchrotron observation of cyclic deformation and phase transformation of superelastic nitinol at ultrasonic frequency. Exp Mech 2020;60:317–28. https://doi.org/10.1007/s11340-019-00562-8.
[13] Fitzka M, Rennhofer H, Catoor D, Reiterer M, Checchia S, di Michiel M, et al. Ultrasonic fatigue of superelastic Nitinol and in situ synchrotron observation of strain and damage. J Mater Res Technol 2024;33:5160–9. https://doi.org/10.1016/J.JMRT.2024.10.172.
[14] McNaney JM, Imbeni V, Jung Y, Papadopoulos P, Ritchie RO. An experimental study of the superelastic effect in a shape-memory Nitinol alloy under biaxial loading. Mech Mater 2003;35:969–86. https://doi.org/10.1016/S0167-6636(02)00310-1.
[15] Mahtabi MJ, Shamsaei N, Mitchell MR. Fatigue of Nitinol: the state-of-the-art and ongoing challenges. J Mech Behav Biomed Mater 2015;50:228–54. https://doi.org/10.1016/j.jmbbm.2015.06.010.
[16] Biffi CA, Fiocchi J, Valenza F, Bassani P, Tuissi A. Selective laser melting of NiTi shape memory alloy: Processability, microstructure, and superelasticity. Shape Mem Superelasticity 2020;6:342–53. https://doi.org/10.1007/s40830-020-00298-8.
[17] ASTM. Standard Test Method for Dynamic Young's Modulus, Shear Modulus, and Poisson's ratio by Impulse Excitation of Vibration. 2015. https://doi.org/10.1520/E1876-15.responsibility.
[18] Pelton AR. Nitinol fatigue: a review of microstructures and mechanisms. J Mater Eng Perform 2011;20:613–7. https://doi.org/10.1007/s11665-011-9864-9.
[19] Concilio A, Antonucci V, Auricchio F, Lecce L, Sacco E. Shape memory alloy engineering: for aerospace, structural, and biomedical applications. Elsevier 2021. https://doi.org/10.1016/B978-0-12-819264-1.01001-3.
[20] Ammar O, Haddar N, Dieng L. Experimental investigation of the pseudoelastic behaviour of NiTi wires under strain- and stress-controlled cyclic tensile loadings. Intermetallics (Barking) 2017;81:52–61. https://doi.org/10.1016/J.INTERMET.2017.03.002.
[21] Nelder JA, Mead R. A simplex method for function minimization. Comput J 1965;7:308–13. https://doi.org/10.1093/comjnl/7.4.308.
[22] Pagnoncelli AP, Tridello A, Paolino DS, Peroni L. Ultrasonic tensile test and micro-CT defect analysis on alumina 99.5%. Mater Des 2024;238:112680. https://doi.org/10.1016/J.MATDES.2024.112680.
[23] Wits WW, Carmignato S, Zanini F, Vaneker THJ. Porosity testing methods for the quality assessment of selective laser melted parts. CIRP Ann Manuf Technol 2016;65:201–4. https://doi.org/10.1016/j.cirp.2016.04.054.
[24] Slotwinski JA, Garboczi EJ, Hebenstreit KM. Porosity measurements and analysis for metal additive manufacturing process control_enhanced reader. J Res Nat Inst Stand Technol 2014:494–528. https://doi.org/10.6028/jres.119.019.
[25] Schild L, Weiser L, Höger K, Lanza G. Analyzing the error of Computed Tomography-based pore detection by using microscope images of matched cross-sections. Precis Eng 2023;81:192–206. https://doi.org/10.1016/J.PRECISIONENG.2023.01.013.
[26] Colombo C, Tridello A, Pagnoncelli AP, Biffi CA, Fiocchi J, Tuissi A, et al. Efficient experimental methods for rapid fatigue life estimation of additive manufactured elements. Int J Fatigue 2023;167:107345. https://doi.org/10.1016/J.IJFATIGUE.2022.107345.
[27] Allegretti D, Berti F, Migliavacca F, Pennati G, Petrini L. Fatigue assessment of nickel–titanium peripheral stents: Comparison of multi-axial fatigue models. Shape Mem Superelasticity 2018;4:186–96. https://doi.org/10.1007/s40830-018-0150-7.
[28] LSTC. LS-DYNA Keyword User's Manual Volume II. 2017.